Journal Pre-proof

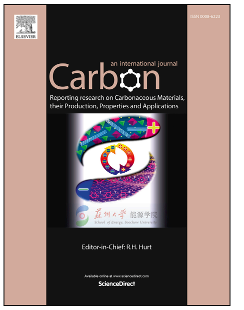

A flexible, scalable, and self-powered mid-infrared detector based on transparent PEDOT: PSS/graphene composite

Mingyu Zhang, John T.W. Yeow

PII: S0008-6223(19)30971-6

DOI: https://doi.org/10.1016/j.carbon.2019.09.062

Reference: CARBON 14632

To appear in: *Carbon*

Received Date: 1 August 2019

Revised Date: 14 September 2019

Accepted Date: 22 September 2019

Please cite this article as: M. Zhang, J.T.W. Yeow, A flexible, scalable, and self-powered mid-infrared detector based on transparent PEDOT: PSS/graphene composite, *Carbon* (2019), doi: https://doi.org/10.1016/j.carbon.2019.09.062.

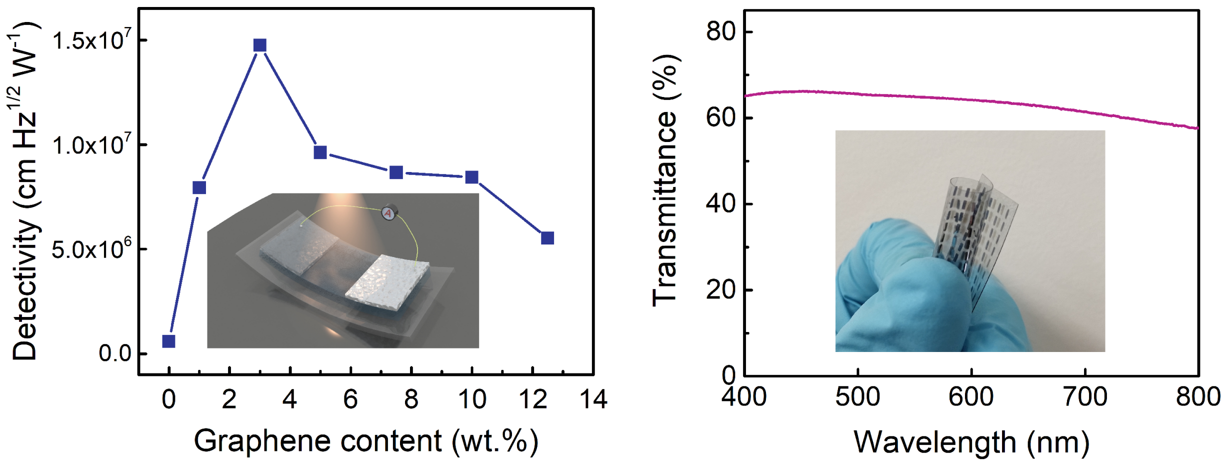
Detectivity (cm Hz^1/2 W^-1)
1.5x10^7
1.0x10^7
5.0x10^6
0.0
0
2
4
6
8
10
12
14
Graphene content (wt.%)
Transmittance (%)
80
60
40
20
0
400
500
600
700
800
Wavelength (nm)

A Flexible, Scalable, and Self-powered Mid-infrared Detector based on Transparent PEDOT: PSS/Graphene Composite

Mingyu Zhang [a], and John T.W. Yeow [a*]

* Corresponding author. Tel: 519-888-4567 x32152. E-mail: jyeow@uwaterloo.ca (John Yeow)

[a] Advanced Micro-/Nano-Devices Lab, Department of Systems Design Engineering, University of Waterloo, 200 University Avenue West, Waterloo, Ontario N2L 3G1, Canada

ABSTRACT

A flexible, self-powered and semi-transparent mid-infrared photodetector is demonstrated with graphene and poly(3,4-ethylenedioxythiophene): poly(4-styrenesulfonate) (PEDOT: PSS) composite on poly vinyl alcohol (PVA) substrate. The effective dispersion of graphene nanoplatelets within polymer chains has yielded a low requisite loading of graphene – only 3 wt.% for the implement of a detector with optimized photo-thermoelectric effect, high flexibility and high transparency. Under a broadband infrared radiation with peak wavelength at 7.8 µm, 1.4×10^7 cm $Hz^{1/2}$ W^{-1} photo detectivity is achieved in composite detector, which is 22 times higher than pure PEDOT: PSS. The demonstrated detector array exhibits good optical transparency of 63% and is capable of being bent to a radius of 1 mm due to strong interaction between composite film and PVA substrate. These features make this scalable mid-infrared photodetector very promising as next-generation optoelectronics.

1. Introduction

Portable and low-cost mid-wave infrared (MWIR, 3–5 µm) and long-wave infrared (LWIR, 8–12 µm) photodetectors meet forthcoming applications in wearable health monitoring electronics, distributed sensor networks in Internet-of-things, and autonomous driving assistants. Traditional mercury cadmium telluride mid-infrared detectors suffer from high material toxicity and fabrication complexity, and state-of-the-art quantum-well photodetectors need be cooled at cryogenic conditions to operate. The advent of novel nanomaterials such as graphene,[1,2] black phosphorus[3,4] and molybdenum disulfide[5] have achieved room-temperature photodetection via mechanisms including bolometric effect,[6] photovoltaic effect,[7] photo-thermoelectric effect (PTE),[8–10] and plasmon detection.[11] As the first 2-D material, graphene exhibits broadband light absorption due to zero bandgap structure and enhanced thermoelectric properties by virtue of low-dimensionality.[32,33] Based on PTE effect, single-layer graphene achieved photo detectivity of ~2×10^{6} cm $Hz^{1/2}$ W^{-1} at 119 μm, and reduced graphene oxide detector exhibited a maximum 4.6×10^{5} cm $Hz^{1/2}$ W^{-1} detectivity in a broadband range from 0.37 to 118 μm.[1,10] Even though large-area graphene growth can be achieved by chemical vapor deposition,[12] high-quality single-layer graphene is expensive for scalable fabrication and fragile to manipulate. CNTs are also ideal PTE materials[26,36–39] and Suzuki *et al.* exemplified a CNT based 1-D detector array for far-infrared imaging with a noise equivalent power less than 1 nW $Hz^{-1/2}$.[13] But drawbacks of pure CNT film detectors are the visible opacity and unstable photocurrent under deformation due to weak Van der Waals interaction between nanotubes.[14]

Modern optoelectronic system expect photodetectors to be low cost and have novel functionalities to accommodate broader applications.[15–17] Polymer based photodetectors are therefore receiving growing attentions in visible and near-infrared range by now due to solution processability, high flexibility, and good transparency.[18–20] PTE conversion is proved with 0.9 mV photovoltage output under 2.3 W cm^{-2} near-infrared excitation in a flexible and transparent hexyl-3,4-ethyl-enedioxyselenophene,[21] - the derivative of PEDOT: PSS which is also investigated as thermoelectric material.[22,23] For MWIR/LWIR regimes, however, polymer based PTE detectors had been vacant until the report of PVA/CNT composite detector by our group in 2018.[14] The rationales of polymer composite based detectors include facile fabrication, improved sensitivity and better flexibility: the composite detector exhibits negligible response variation at 3.5 mm bending radius while the responsivity sees several times improvement with detectivity of 4.9×10^{6} cm $Hz^{1/2}$ W^{-1}, attributed to the interface phonon scattering and energy filtering effects.[24–28] However, PVA/CNT composite is opaque and unoptimized due to aggregation induced high CNT loading.[14,29,30]

In this work, we have developed a unique and facile fabrication technique towards a flexible, scalable, self-powered, and semi-transparent mid-infrared photodetector using PEDOT: PSS/graphene composite. An optimized photoresponse is achieved at a low loading of graphene (3 wt.%) in polymer composite and 1.4×10^{7} cm $Hz^{1/2}$ W^{-1} photo detectivity under broadband mid-infrared radiation has been measured in an asymmetric PTE architecture. To the best of our knowledge, this is the firstly demonstrated flexible, semi-transparent, and self-powered mid-infrared photodetector to date.

2. Experimental Section

2.1 Synthesis of PEDOT: PSS/graphene Nanoplatelets Composite

0.5 mL Dimethyl sulfoxide (purchased from Sigma-Aldrich, product ID: D4540) which acts as electrical conductivity enhancer is first added into 10 mL PEDOT: PSS water solution (1.3 wt.%, purchased from Sigma-Aldrich, product ID: 483095, and the ratio between PEDOT and PSS is 5:8). Next, graphene nanoplatelets (7 nm thickness, 2 µm diameter, purchased from Kennedy Labs) with different loadings within the composite (0 wt.%, 1 wt.%, 3 wt.%, 5 wt.%, 7.5 wt.%, 10 wt.%, 12.5 wt.%) are added into PEDOT: PSS solution. The mixed solution is dispersed by magnetic stirring at room temperature for 3 hours and placed in an ultrasonic bath (50 W) for 15 min in order to reduce the π-π stacking between graphene flakes. Dispersed solution is then transferred onto Kapton substrate (polyimide, ~100 µm thick) that has been pre-treated by 10%

HCl solution for 1 hour to improve the hydrophilicity. A typically 3~4 μm thick and non-transparent graphene/PEDOT: PSS film can be obtained through drop-casting followed by 1 hour annealing at 150 □ on hot-plate.

For a transparent and highly flexible composite (film thickness 0.1~1 μm), the synthesis process is shown in Figure 1. Dispersed PEDOT: PSS/graphene solution is first spin-coated onto HCl treated Kapton substrate at 500 ~ 2000 rpm speed followed by 10 min annealing at 150 □. Next, a relatively sticky PVA (100,000 molecular weight, 87% hydrolyzed, purchased from Fischer Scientific) water solution is drop casted onto the dry PEDOT: PSS/graphene composite surface. The hybrid material is left drying in ambient condition for over 48 hours. Finally, the PEDOT: PSS/graphene will stick with the PVA sheet and easily peel off the Kapton substrate attributed to the similar hydrophilic properties of PVA and PEDOT: PSS.

Journal Pre-proof

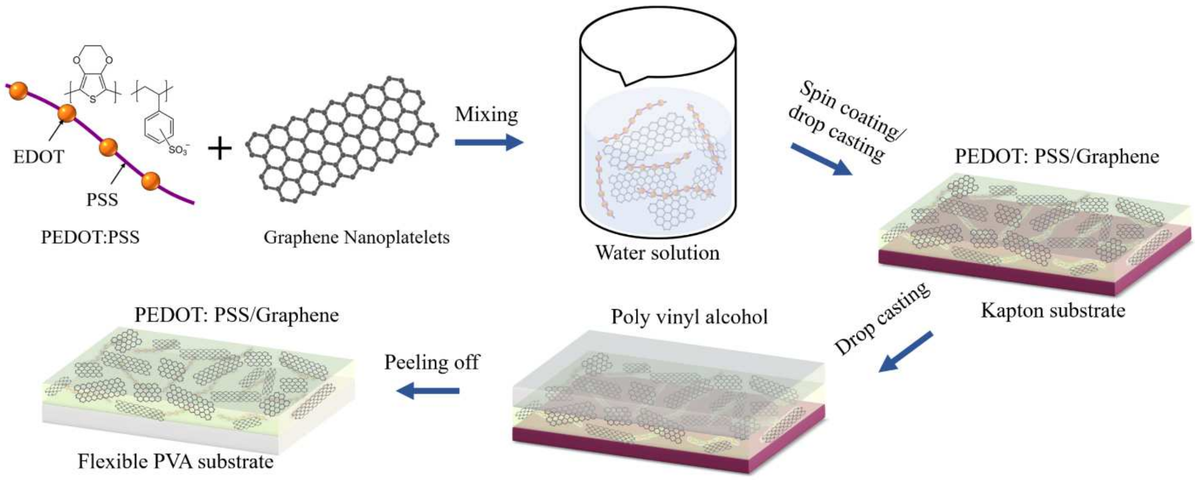

Figure 1. Solution processing of the flexible and semi-transparent PEDOT: PSS/graphene composite on PVA substrate.

2.2 Characterizations of PEDOT: PSS/graphene Nanoplatelets Composite

Scanning electron microscopy (SEM) images was taken in a JEOL JSM 7200F field emission SEM at 10 kV voltage and 9 nA beam current. The Fourier Transform Infrared Spectroscopy (FTIR) spectra were measured in Bruker Tensor 27 FTIR system. The Raman spectra were obtained in Bruker Senterra-2 Raman spectrometer. The UV-Vis spectra of PEDOT: PSS/graphene composite were obtained in a PerkinElmer Lambda 35 &1050 UV-Vis spectrometer.

2.3 Device Fabrication and Characterization

On top of PEDOT: PSS/graphene composite, 200 nm aluminum (Al) and 25 nm indium tin oxide (ITO) electrodes are formed via and magnetron sputter deposition, as shown in Figure 2a. Shadow mask is used to pattern the electrodes rather than photo lithography or electron-beam lithography,. For the semi-transparent devices, a thinner Al electrode layer - 15 nm (or 25 nm) is used instead of 200 nm. A 13×13 pixeled detector array with 2.8 mm pixel-size is also fabricated with shadow mask technique.

For detector characterization, we use low-intensity, broadband blackbody radiation source (Newport Oriel 67030) instead of high-power lasers in order to imitate the real-world mid-infrared radiation. The black-body temperature is set from 373 K to 573 K with an opening spot diameter of 0.5 cm or 1 cm, and the photodetector devices to be characterized are placed 25 mm away from the opening. The I−V characteristics with and without black-body illumination were measured by a Keithley 6487 pico-ammeter. The photo-thermoelectric voltages at zero-bias were calculated from measured photocurrents by $V = IR$ where R represents resistance of the device.

3. Results and discussion

3.1 Device schematic and photoresponse

The SEM image (Figure S1), FTIR spectra (Figure S2), and Raman spectra (Figure S3) of as-synthesized composites show that the graphene nanoplatelets have been effectively dispersed within PEDOT: PSS polymer matrix (as discussed in Supplementary Information). This is considered the main reason for achieving optimized PTE performance at relatively low graphene loading. Figure 2b and Figure S4 show the temporal responses of the PEDOT: PSS/graphene photodetector placed on Kapton substrate, and Figure 2c illustrates schematic of the device under infrared radiation. The blackbody infrared source is set at 573 K and the detector received power density is 225 μW mm^{-1}. A relatively long photocurrent transition time of 15~30 s has been observed since a stable photocurrent response can be achieved only when the thermal equilibrium is established among channel, substrate and environment. Figure 2d shows the current-voltage curves of the photodetector under dark condition and under blackbody illuminated conditions where a net photocurrent is measured at zero voltage bias.

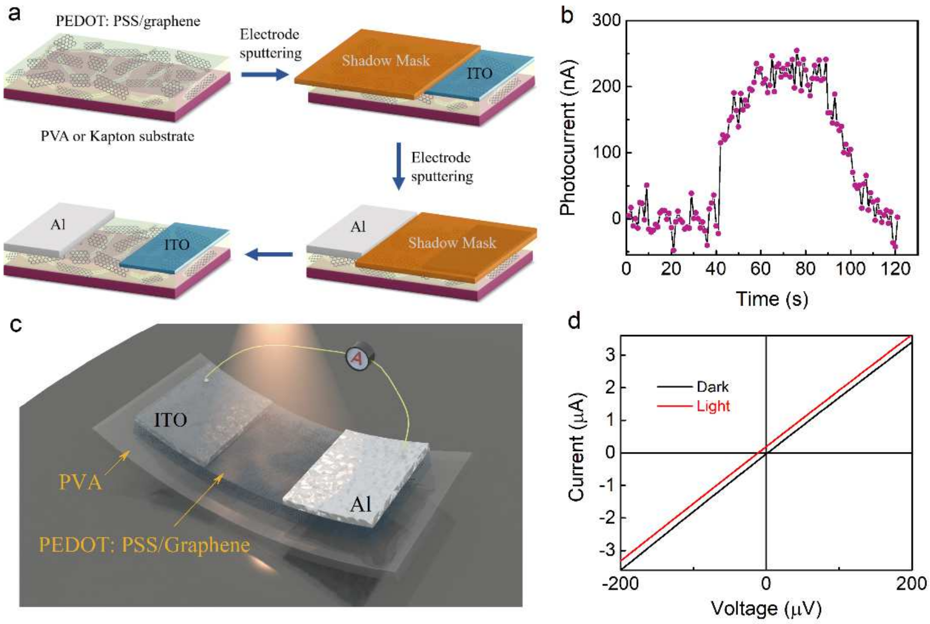

Figure 2. a, Non-lithographic fabrication processes of the PEDOT: PSS/graphene based photodetector. **b**, Temporal response of 3 wt.% graphene loading photodetector under 225 μW mm^{-1} blackbody radiation. **c,** Schematic of the flexible, semi-transparent infrared detector. **d**, I-V curves of the photodetector measured in the dark and under blackbody illumination.

3.2 Photoresponse regarding graphene loading and incident infrared power

The photo-thermoelectric characteristics of PEDOT: PSS/graphene detectors have been investigated by tuning the graphene nanoplatelets content within composite. The electrical resistance has seen a 9-fold reduction in the polymer even with 1 wt.% graphene loading (Figure S5). The self-powered, zero-bias property of PTE mechanism is known to reduce the detector noise significantly,[13,31] and an important reason to achieve room temperature photodetection. The detectivity $D^* = \frac{R_V\sqrt{A}}{V_n}$ which represents the capability of identifying the weakest photons from the noise is used to evaluate the photodetector performance where $R_V = V/P$ is voltage responsivity, V is photo induced voltage, P is incident power, A is photosensitive area, and V_n is the noise voltage.[13] The main noise floor in zero-biased detector is the Johnson-Nyquist noise $V_n = \sqrt{4k_BTR}$ where k_B is Boltzmann constant, *T* is temperature, and *R* is resistance.[1,13]

It is considered that despite being a superior light absorbing material, graphene is not an efficient thermoelectric material because of the high thermal conductivity. When graphene is blended with organic polymer, however, the composite thermal conductivity can be significantly reduced (approaching to the level of thermally insulating polymers).[17] Therefore, improved figure of merit for thermoelectric materials - *ZT* value can be achieved

$$ZT = \frac{\sigma S^2 T}{\kappa} \tag{1}$$

where σ is electrical conductivity, κ is thermal conductivity, *S* is Seebeck coefficient, and *T* is temperature. For pure PEDOT: PSS based device (0 wt.% graphene), the photo detectivity is only 5.9×10^5 cm $Hz^{1/2}$ W^{-1} at 55 μW mm^{-1} radiation as shown in Figure 3. By increasing the graphene loading from 0 wt.% to 3 wt.%, the detectivity increases by 22 folds to 1.3×10^7 cm $Hz^{1/2}$ W^{-1} under the same illumination condition. We explain this phenomenon with two reasons: 1) enhanced photo absorption at elevated graphene loading within composite, 2) optimized thermoelectric efficiency at 2~3 wt.% graphene loading due to efficient phonon scattering and energy filtering effect as reported by literature on PEDOT: PSS composite.[29,32,33] When the graphene loading increases from 3 wt.% to 12.5 wt.%, the photoresponse is found decreasing. The reduction is assumed correlated to the increased thermal conductivity at elevated graphene loading[34] and reduced Seebeck coefficient due to higher carrier concentrations as explained by[29,32]

$$S = \frac{8L}{h^2} m^* T \left(\frac{\pi}{3n}\right)^{2/3} \tag{2}$$

where $L = \pi^2 k_B^2 / 3e^2$ is the Lorentz number, h is Planck constant, m^* is effective mass of the carrier, and n is carrier concentration.

The optimized PTE performance can be achieved at such low graphene content because the PEDOT: PSS chains have facilitated the dispersion of graphene. A strong π-π interaction exists between the 2D graphene nanoplatelets and the planar backbone of PEDOT, and an intermolecular electrostatic repulsive force also exists between PSS and the graphene.[29] As a comparison to PEDOT: PSS/CNT composite, the optimized CNT loading is much higher - typically 35 wt.%, due to the bundling and aggregation of cylinder-shaped CNTs.[29,35] The implications of low requisite graphene loading include better material biocompatibility [36,37], lower cost, and the possibility to integrate highly-transparent and ultra-flexible devices.

Figure 3b shows the photodetector responses under various blackbody radiation conditions. While the temperature of blackbody source decreases from 573 K to 373 K, i.e. detector received power density decreases from 225 µW mm^{-1} to 26.5 µW mm^{-1} (the spectral radiant emittances are shown in Figure S6), the detector photoresponse sees a small increase from 1.1×10^7 cm $Hz^{1/2}$ W^{-1} to 1.4×10^7 cm $Hz^{1/2}$ W^{-1}. This variation is attributed to the reduced efficiency of thermal diffusion in the channel/substrate at a stronger infrared radiation. Compared to our previous work using PVA/CNT composite, the PEDOT: PSS/graphene photoresponse exhibits an increase of 2.9 folds.[14] We explain the improvement by two reasons: 1) optimized electrode design – replacing 200 nm titanium with 25 nm ITO which leads to enhanced PTE asymmetry in terms of light reflection, thermal conduction, and Seebeck coefficient,[38] 2) the effective dispersion of graphene which contributes to a higher thermoelectric conversion efficiency compared to CNT composite.[29]

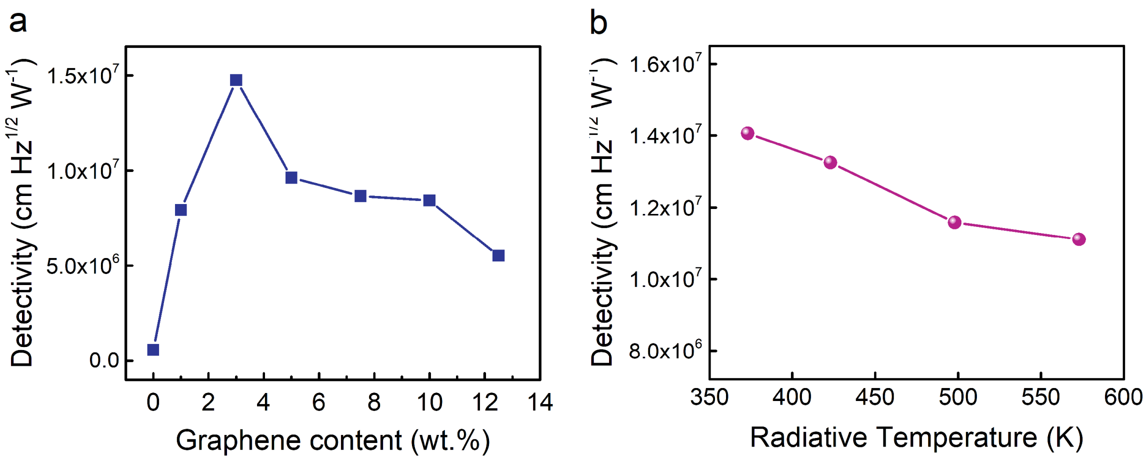

Figure 3. a, Photodetector detectivity correlation with the increasing graphene content within the PEDOT: PSS/graphene composite. The graphene nanoplatelets loadings are 0 wt.%, 1 wt.%, 3 wt.%, 5 wt.%, 7.5 wt.%, 10 wt.%, 12.5 wt.%, respectively. **b**, The photoresponse of 3 wt.% graphene photodetector at different blackbody radiation temperatures. While the radiative temperatures are 373 K, 423 K, 498 K, 573 K, the detector received power densities are 26.5 μW mm^{-1}, 54.9 μW mm^{-1}, 121 μW mm^{-1}, 225 μW mm^{-1}, respectively.

3.3 Photoresponse regarding composite thickness

We further investigated the photoresponse of PEDOT: PSS/graphene composites with various film thicknesses. The as-prepared PEDOT: PSS/3 wt.% graphene solution is spin-coated at 500 rpm, 1000 rpm, 1500 rpm and 2000 rpm, and the corresponding thicknesses are 1000 nm, 450 nm, 250 nm and 100 nm, respectively. The composite film obtained by drop-casting is typically much thicker - around 3 μm. Figure 4 shows the photoresponse correlation with different thicknesses of the composite, and the maximum voltage responsivity is found in the 450 nm thick film obtained at 1000 rpm coating speed. The responsivity trend with composite thickness could be understood by a theoretical model:[38]

$$V_{half} = S_{\text{total}}(T_{\text{electrode}} - T_{\text{interface}}) + S_{\text{composite}}(T_{\text{interface}} - T_{\text{composite}}) \quad (3)$$

$$S_{\text{total}} = \frac{\sigma_{\text{electrode}} t_{\text{electrode}} S_{\text{electrode}} + \sigma_{\text{composite}} t_{\text{composte}} S_{\text{composite}}}{\sigma_{\text{electrode}} t_{\text{electrode}} + \sigma_{\text{composite}} t_{\text{composite}}} \tag{4}$$

where V_{half} is the photo voltage generated by half of the photodetector as shown in Figure 4b, S_{total} is the overall Seebeck coefficient of the electrode and composite underneath (substrate included), $T_{\text{interface}}$ is the temperature at the electrode/composite interface, and $T_{\text{electrode}}$ and $T_{\text{composite}}$ are the temperatures at two farther-ends of the electrode and composite, respectively. Equation (3, 4) indicate that the dimensions of films are correlated to the thermoelectric voltage in several ways: the thicknesses of the electrode and the composite could affect the light absorption, the channel temperature gradient and determines the S_{total}. Other factors causing the reduced photoresponse in thinner composite film, for instance in the 100 nm thick film, could be the phase separation between PEDOT and PSS chains at high coating speed,[39,40] or the change of disperse state of graphene nanoplatelets (2 μm diameter) within polymers. The high detectivity in the 3000 nm composite (drop-casted) device, however, is due to the reduced electrical resistance as $D^* \propto R^{-1/2}$.[31]

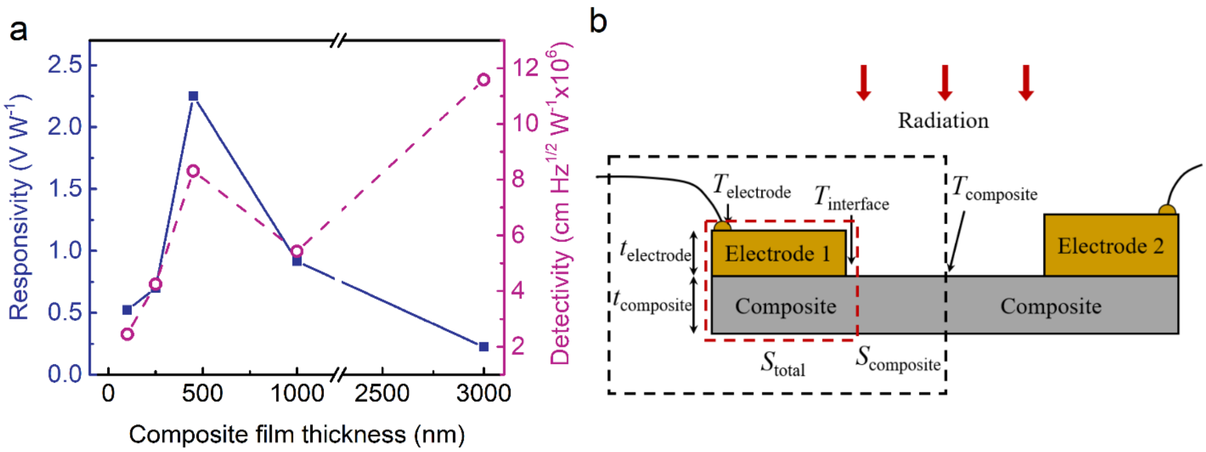

Figure 4. a, Photoresponsivity correlation with PEDOT: PSS/graphene composite film thickness. **b**, A schematic of the detector whose photoresponse is related to the temperatures and Seebeck coefficients in some of its parts. The electrodes are 25 nm Al and 25 nm ITO.

3.4 Semi-transparent photodetectors

Next, semi-transparent photodetectors are demonstrated by transferring the spin-coated composite onto transparent PVA substrate and integrating thin electrodes. The optical image and UV-Vis transmittance spectrum of PVA supported PEDOT: PSS/graphene composite are presented in Figure 5a, which exhibit 80% light transmittance in 400 ~ 800 nm visible range. The optical transmittance is 61% (or 59%) for the device with 15 nm Al (or 25 nm) and 25 nm ITO electrodes, (Figure 5b), and 63% for the 13×13 pixeled detector array (Figure 5c). It is apparent that the main limitation of detector transparency is the reflective Al metal film, and a possible way to mitigate this is to replace the continuous film with conductive nanowire network.[41,42] It is noteworthy that with thinner Al electrode (20 nm), the photoresponse of the device exhibits certain degradation compared to that with a thicker electrode (200 nm).[13] Still, a relatively high detectivity of 8.3×10^{6} cm $Hz^{1/2}$ W^{-1} is achieved in the 25 nm Al and 25 nm ITO device, and 7.0×10^{6} cm $Hz^{1/2}$ W^{-1} is achieved in the 15 nm Al and 25 nm ITO device, which are comparable to non-transparent photodetectors. The comparison between this work and representative room temperature MWIR/LWIR detectors is shown in Table S1 and a comparison of polymer (composite) based PTE detectors are shown in Table S2.

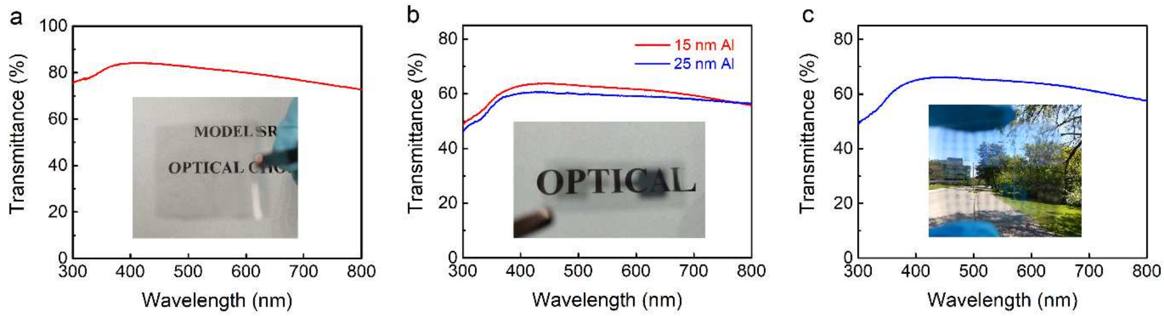

Figure 5. Transparent composite and semi-transparent photodetectors. **a**, The UV-Vis spectrum and optical image of the PEDOT: PSS/graphene composite on PVA substrate in visible range. **b**, The UV-Vis spectra of composite based photodetectors with 15 nm/25 nm Al and 25 nm ITO as electrodes. The optical image is the 15 nm Al electrode based device. **c**, The UV-Vis spectrum and optical image of a 13×13 pixeled detector array.

3.5 Detector flexibility

The PEDOT: PSS/graphene detector exhibits excellent flexibility and stable photoresponse under bending deformation. Figure 6a shows the photoresponse output at different bending radiuses in a drop-casted 3 wt.% graphene composite on Kapton substrate. The photoresponse only exhibits a small change at a significant bending of 1 cm radius. We presume the stable response originates from a strong interaction between graphene filler and polymer matrix that is important in maintaining certain electrical and thermal transport paths.[14] However, due to the excessive thickness of the composite and its weak interaction with Kapton substrate, several cracks appeared on the composite film after 100 times bending. But this issue is significantly mitigated in the spin-coated composite film that is transferred onto a flexible PVA substrate. Figure 6b shows a good photoresponse endurance of a PVA supported, spin-coated composite during 400 times bending. The photo voltages are measured under flat state of the device after each bending. Thanks to high flexibility of the thin composite itself and its strong interaction to the PVA substrate (both hydrophilic materials), quite small bending radius below 1 mm is achieved in a single pixel detector (Figure 6c) and a 13×13 pixeled array (Figure 6d).

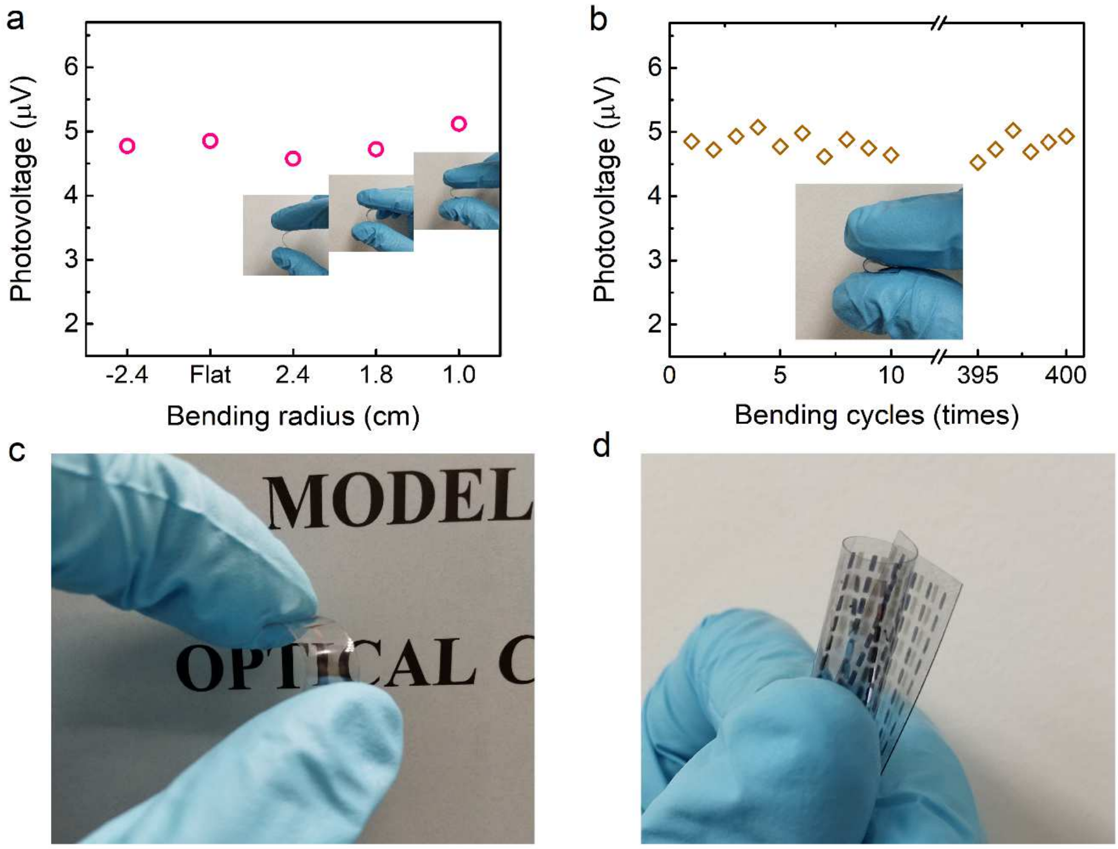

Figure 6. Bending properties of PEDOT: PSS/graphene based photodetectors. **a**, The photovoltage outputs of a device on Kapton substrate at convex bending of 2.4 cm, 1.8 cm, 1.0 cm radiuses, and concave bending of 2.4 cm radius. **b**, Photovoltage outputs during 400 times bending to 1 mm radius. **c**, **d**, Optical images of the flexible, semi-transparent single-pixel detector and detector array.

3.6 Response to infrared radiation from human body

Finally, human-body passive radiation detection is performed using the PEDOT: PSS/3 wt.% graphene detector. Similar to the blackbody source we use for characterization, thermal emission from human-body is a broadband radiation covering MWIR and LWIR regimes having peak wavelength at 9.3 μm. A notable photocurrent is observed under the unfocused, spontaneous body emission when the fingertip is placed ~2 mm away from the detector as shown in Figure 7a. This demonstrates the possible functionality of this device as wearable optoelectronics since the fluctuation of body radiation could be reflected in the change of photocurrent. Figure 7b presents a flexible, transparent wristband integrated with a single-pixel PEDOT: PSS/graphene detector. By tracking the variation of body emission, the wristband can serve as a wearable monitor for the sleep health condition.[43,44] Wearable MWIR/LWIR detectors can also diagnose breast or skin cancers and foot ulcerations attributed to the infrared radiation change from the body at their very early occurrence.[45,46] We consider our photodetector have advantages in terms of comfort, convenience, and integration compared to skin-touching, rigid, and battery-driven temperature sensors. Furthermore, Figure S7a-c show possible applications of a flexible and semi-transparent 13×13 pixeled detector array, which is proposed as part of the gesture recognition system inside vehicles as a supplement to the current ultrasound transducers, or as photodetector/energy-harvester installed on the car windshield of the environmental MWIR/LWIR radiation. Since the infrared emissivity of various matters such as bio-tissues are different (even under the same temperature), the detector array could also be integrated onto glasses/contact lens and serve as eyeball tracking device under dark conditions.

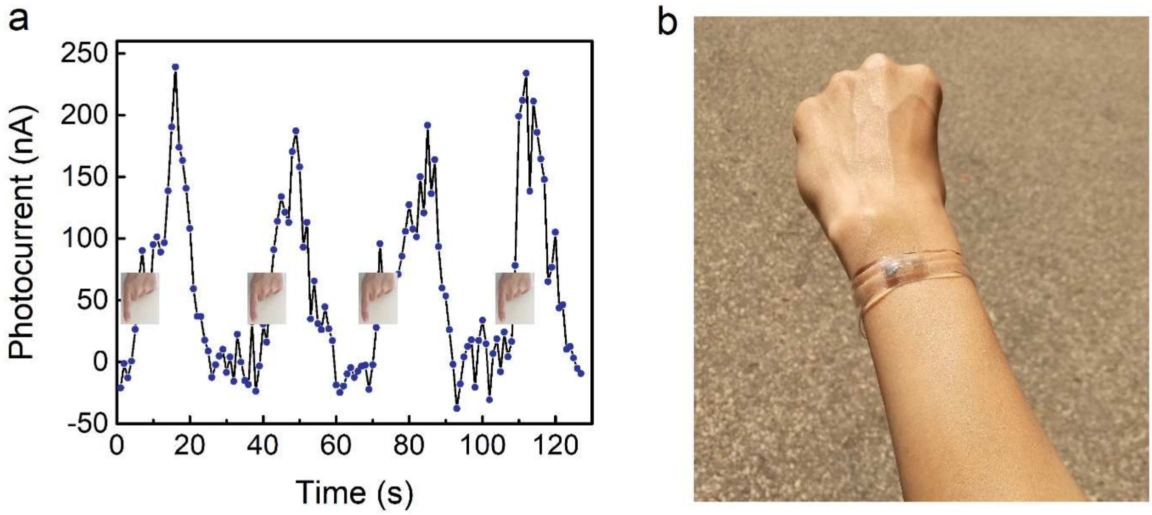

Figure 7. a, Repeated detection of a human fingertip radiation placed above the detector surface without contact. The device is drop-casted PEDOT: PSS/3 wt.% graphene with 200 nm Al. **b**, A flexible, semi-transparent wrist belt with the self-powered photodetector integrated.

4. Conclusion

In summary, PEDOT: PSS/graphene composite mid-infrared photodetectors have been demonstrated based on self-powered photo-thermoelectric effect. This flexible, semi-transparent, and sensitive photodetector is fabricated by a unique, scalable method. The best photo detectivity of 1.4×10^{7} cm $Hz^{1/2}$ W^{-1} is achieved at a graphene loading of 3 wt.% within PEDTO: PSS. High flexibility at the bending radius of 1 mm, high optical transmittance - 80% for the composite and 63% for detector array have been achieved. These photodetector functionalities could open new possibilities of next-generation optoelectronics for applications in Internet-of-things sensors, wearable biomedical electronics, and autonomous driving assistants.

Supplementary Information

Supplementary Information is available.

Acknowledgements

This work is supported by the Natural Sciences and Engineering Research Council of Canada (NSERC), Canada Research Chairs program (CRC) to Prof. J.Y., and CMC Micro- systems Micro-Nano Technology (MNT) Financial Assistance (project reference ID: 6610). The authors acknowledge Prof. Dayan Ban for allowing us to use the blackbody source in his lab.

Competing interests: The authors declare that they have no competing interests.

ORCID
Mingyu Zhang: 0000-0003-3531-7369
John T.W. Yeow: 0000-0002-0740-8055

References

[1] X. Cai, A.B. Sushkov, R.J. Suess, M.M. Jadidi, G.S. Jenkins, L.O. Nyakiti, et al., Sensitive room-temperature terahertz detection via the photothermoelectric effect in graphene, Nat. Nanotechnol. 9 (2014) 814–819. doi:10.1038/nnano.2014.182.

[2] L. Vicarelli, M.S. Vitiello, D. Coquillat, a. Lombardo, a. C. Ferrari, W. Knap, et al., Graphene field-effect transistors as room-temperature terahertz detectors, Nat. Mater. 11 (2012) 865–871. doi:10.1038/nmat3417.

[3] X. Chen, X. Lu, B. Deng, O. Sinai, Y. Shao, C. Li, et al., Widely tunable black phosphorus mid-infrared photodetector, Nat. Commun. 8 (2017) 1672–1678. doi:10.1038/s41467-017-01978-3.

[4] M. Long, A. Gao, P. Wang, H. Xia, C. Ott, C. Pan, et al., Room temperature high-detectivity mid-infrared photodetectors based on black arsenic phosphorus, Sci. Adv. 3 (2017). doi:10.1126/sciadv.1700589.

[5] J. Bullock, M. Amani, J. Cho, Y. Chen, G.H. Ahn, V. Adinolfi, et al., Polarization-

resolved black phosphorus/molybdenum disulfide mid-wave infrared photodiodes with high detectivity at room temperature, Nat. Photonics. 12 (2018) 601–607. doi:10.1038/s41566-018-0239-8.

[6] J. Yan, M.-H. Kim, J. a. Elle, a. B. Sushkov, G.S. Jenkins, H.M. Milchberg, et al., Dual-gated bilayer graphene hot-electron bolometer, Nat. Nanotechnol. 7 (2012) 472–478. doi:10.1038/nnano.2012.88.

[7] X. Yu, Y. Li, X. Hu, D. Zhang, Y. Tao, Z. Liu, et al., Narrow bandgap oxide nanoparticles coupled with graphene for high performance mid-infrared photodetection, Nat. Commun. 9 (2018) 4299. doi:10.1038/s41467-018-06776-z.

[8] S. Castilla, B. Terrés, M. Autore, L. Viti, J. Li, A.Y. Nikitin, et al., Fast and Sensitive Terahertz Detection Using an Antenna-Integrated Graphene pn Junction, Nano Lett. 19 (2019) 2765−2773. doi:10.1021/acs.nanolett.8b04171.

[9] M. Badioli, A. Woessner, K.J. Tielrooij, S. Nanot, G. Navickaite, T. Stauber, et al., Phonon-mediated mid-infrared photoresponse of graphene, Nano Lett. 14 (2014) 6374–6381. doi:10.1021/nl502847v.

[10] J. Wen, Y. Niu, P. Wang, M. Chen, W. Wu, Y. Cao, et al., Ultra-broadband self-powered reduced graphene oxide photodetectors with annealing temperature-dependent responsivity, Carbon. 153 (2019) 274–284. doi:10.1016/j.carbon.2019.07.033.

[11] Q. Guo, R. Yu, C. Li, S. Yuan, B. Deng, F.J.G. de Abajo, et al., Efficient Electrical Detection of Mid-Infrared Graphene Plasmons at Room Temperature, Nat. Mater. 17 (2018) 986–992. doi:10.1038/s41563-018-0157-7.

[12] T. Wu, X. Zhang, Q. Yuan, J. Xue, G. Lu, Z. Liu, et al., Fast Growth of Inch-sized Single

Crystalline Graphene from a Controlled Single Nucleus on Cu-Ni Alloy, Nat. Mater. 15 (2015) 43–47. doi:10.1038/nmat4477.

[13] D. Suzuki, S. Oda, Y. Kawano, A flexible and wearable terahertz scanner, Nat. Photonics. 10 (2016) 809–813. doi:10.1038/nphoton.2016.209.

[14] M. Zhang, J.T.W. Yeow, Flexible Polymer - Carbon Nanotube Composite with High Response Stability for Wearable Thermal Imaging, ACS Appl. Mater. Interfaces. 10 (2018) 26604–26609. doi:10.1021/acsami.8b06482.

[15] H. Kim, J.H. Ahn, Graphene for flexible and wearable device applications, Carbon. 120 (2017) 244–257. doi:10.1016/j.carbon.2017.05.041.

[16] X. Zhao, Q. Zhang, D. Chen, P. Lu, Enhanced mechanical properties of graphene-based polyvinyl alcohol composites, Macromolecules. 43 (2010) 2357–2363. doi:10.1021/ma902862u.

[17] X. Sun, H. Sun, H. Li, H. Peng, Developing polymer composite materials: Carbon nanotubes or graphene?, Adv. Mater. 25 (2013) 5153–5176. doi:10.1002/adma.201301926.

[18] S.F. Leung, K.T. Ho, P.K. Kung, V.K.S. Hsiao, H.N. Alshareef, Z.L. Wang, et al., A Self-Powered and Flexible Organometallic Halide Perovskite Photodetector with Very High Detectivity, Adv. Mater. 30 (2018) 1–8. doi:10.1002/adma.201704611.

[19] G. Pace, A. Grimoldi, D. Natali, M. Sampietro, J.E. Coughlin, G.C. Bazan, et al., All-organic and fully-printed semitransparent photodetectors based on narrow bandgap conjugated molecules, Adv. Mater. 26 (2014) 6773–6777. doi:10.1002/adma.201402918.

[20] H. Zhang, S. Jenatsch, J. De Jonghe, F. Nuësch, R. Steim, A.C. Véron, et al., Transparent organic photodetector using a near-infrared absorbing cyanine dye, Sci. Rep. 5 (2015) 1–6.

doi:10.1038/srep09439.

[21] B. Kim, H. Shin, T. Park, H. Lim, E. Kim, NIR-sensitive poly(3,4-ethylenedioxyselenophene) derivatives for transparent photo-thermo-electric converters, Adv. Mater. 25 (2013) 5483–5489. doi:10.1002/adma.201301834.

[22] T.G. Novak, H. Shin, J. Kim, K. Kim, A. Azam, C.V. Nguyen, et al., Low-Cost Black Phosphorus Nanofillers for Improved Thermoelectric Performance in PEDOT:PSS Composite Films, ACS Appl. Mater. Interfaces. 10 (2018) 17957–17962. doi:10.1021/acsami.8b03982.

[23] Z. Fan, J. Ouyang, Thermoelectric Properties of PEDOT:PSS, Adv. Electron. Mater. 1800769 (2019) 1–23. doi:10.1002/aelm.201800769.

[24] M. He, F. Qiu, Z. Lin, Towards high-performance polymer-based thermoelectric materials, Energy Environ. Sci. 6 (2013) 1352–1361. doi:10.1039/c3ee24193a.

[25] M. Ibáñez, Z. Luo, A. Genç, L. Piveteau, S. Ortega, D. Cadavid, et al., High-performance thermoelectric nanocomposites from nanocrystal building blocks, Nat. Commun. 7 (2016) 10766. doi:10.1038/ncomms10766.

[26] B.T. McGrail, A. Sehirlioglu, E. Pentzer, Polymer composites for thermoelectric applications, Angew. Chemie - Int. Ed. 54 (2015) 1710–1723. doi:10.1002/anie.201408431.

[27] Y. Chen, M. He, B. Liu, G.C. Bazan, J. Zhou, Z. Liang, Bendable n-Type Metallic Nanocomposites with Large Thermoelectric Power Factor, Adv. Mater. 29 (2017) 1604752.

[28] K. Suemori, Y. Watanabe, S. Hoshino, Carbon nanotube bundles/polystyrene composites

as high-performance flexible thermoelectric materials, Appl. Phys. Lett. 106 (2015) 113902. doi:10.1063/1.4915622.

[29] G.H. Kim, D.H. Hwang, S.I. Woo, Thermoelectric properties of nanocomposite thin films prepared with poly(3,4-ethylenedioxythiophene) poly(styrenesulfonate) and graphene, Phys. Chem. Chem. Phys. 14 (2012) 3530–3536. doi:10.1039/c2cp23517j.

[30] T. Ramanathan, A.A. Abdala, S. Stankovich, D.A. Dikin, M. Herrera-Alonso, R.D. Piner, et al., Functionalized graphene sheets for polymer nanocomposites, Nat. Nanotechnol. 3 (2008) 327–331. doi:10.1038/nnano.2008.96.

[31] K.W. Mauser, S. Kim, S. Mitrovic, D. Fleischman, R. Pala, K.C. Schwab, et al., Resonant thermoelectric nanophotonics, Nat. Nanotechnol. 12 (2017) 770–775. doi:10.1038/nnano.2017.87.

[32] D. Yoo, J. Kim, J.H. Kim, Direct synthesis of highly conductive poly(3,4-ethylenedioxythiophene):Poly(4-styrenesulfonate) (PEDOT:PSS)/graphene composites and their applications in energy harvesting systems, Nano Res. 7 (2014) 717–730. doi:10.1007/s12274-014-0433-z.

[33] F. Li, K. Cai, S. Shen, S. Chen, Preparation and thermoelectric properties of reduced graphene oxide/PEDOT:PSS composite films, Synth. Met. 197 (2014) 58–61. doi:10.1016/j.synthmet.2014.08.014.

[34] D. Yoo, J. Kim, S.H. Lee, W. Cho, H.H. Choi, F.S. Kim, et al., Effects of one- and two-dimensional carbon hybridization of PEDOT : PSS on the power factor of polymer thermoelectric energy conversion devices, J. Mater. Chem. A. 3 (2015) 6526–6533. doi:10.1039/c4ta06710j.

[35] D. Kim, Y. Kim, K. Choi, J.C. Grunlan, C. Yu, Improved thermoelectric behavior of nanotube-filled polymer composites with poly(3,4-ethylenedioxythiophene) poly(styrenesulfonate), ACS Nano. 4 (2010) 513–523. doi:10.1021/nn9013577.

[36] A. Bianco, K. Kostarelos, M. Prato, Making carbon nanotubes biocompatible and biodegradable, Chem. Commun. 47 (2011) 10182–8. doi:10.1039/c1cc13011k.

[37] H.J. Salavagione, A.M. Díez-Pascual, E. Lázaro, S. Vera, M. a. Gómez-Fatou, Chemical sensors based on polymer composites with carbon nanotubes and graphene: the role of the polymer, J. Mater. Chem. A. 2 (2014) 14289–14328. doi:10.1039/C4TA02159B.

[38] D. Suzuki, Y. Ochiai, Y. Kawano, Thermal Device Design for a Carbon Nanotube Terahertz Camera, ACS Omega. 3 (2018) 3540–3547. doi:10.1021/acsomega.7b02032.

[39] D. Yoo, W. Son, S. Kim, J.J. Lee, S.H. Lee, H.H. Choi, et al., Gradual thickness-dependent enhancement of the thermoelectric properties of PEDOT:PSS nanofilms, RSC Adv. 4 (2014) 58924–58929. doi:10.1039/c4ra09587a.

[40] C. Park, D. Yoo, S. Im, S. Kim, W. Cho, J. Ryu, et al., Large-scalable RTCVD Graphene/PEDOT:PSS hybrid conductive film for application in transparent and flexible thermoelectric nanogenerators, RSC Adv. 7 (2017) 25237–25243. doi:10.1039/c7ra02980b.

[41] J.Y. Lee, S.T. Connor, Y. Cui, P. Peumans, Solution-processed metal nanowire mesh transparent electrodes, Nano Lett. 8 (2008) 689–692. doi:10.1021/nl073296g.

[42] S. Nanowire, L. Hu, H.S. Kim, J. Lee, P. Peumans, Y. Cui, Scalable Coating and Properties of Transparent, Flexible, Silver Nanowire Electrodes, ACS Nano. 4 (2010) 2955–2963.

[43] J.A. Sarabia, M.A. Rol, P. Mendiola, J.A. Madrid, Circadian rhythm of wrist temperature in normal-living subjects. A candidate of new index of the circadian system, Physiol. Behav. 95 (2008) 570–580. doi:10.1016/j.physbeh.2008.08.005.

[44] A. Sano, R.W. Picard, R. Stickgold, Quantitative analysis of wrist electrodermal activity during sleep, Int. J. Psychophysiol. 94 (2014) 382–389. doi:10.1016/j.ijpsycho.2014.09.011.

[45] B.B. Lahiri, S. Bagavathiappan, T. Jayakumar, J. Philip, Medical applications of infrared thermography: A review, Infrared Phys. Technol. 55 (2012) 221–235. doi:10.1016/j.infrared.2012.03.007.

[46] R. Gade, T.B. Moeslund, Thermal cameras and applications: A survey, Mach. Vis. Appl. 25 (2014) 245–262. doi:10.1007/s00138-013-0570-5.